LAWRENCE
LIVERMORE
NATIONAL
LABORATORY

UCRL-JRNL-207238

An Orientation Distribution Function for Trabecular Bone

J.H.Kinney, J.S.Stolken, T.S.Smith, J.T.Ryaby, N.E.Lane

October 15, 2004

Bone

An Orientation Distribution Function for Trabecular Bone

John H. Kinney, James S. Stölken, T.S. Smith
Department of Mechanical Engineering
Lawrence Livermore National Laboratory

James T. Ryaby
Research and Development
OrthoLogic Corp.
Tempe, AZ 85281

N.E. Lane
Department of Medicine
University of California, San Francisco

Prepared for submittal as Technical Note to *Bone*

Corresponding Author:

J.H. Kinney
UCSF/UCB Joint Graduate Group in Bioengineering
Department of Mechanical Engineering
Lawrence Livermore National Laboratory
Livermore, CA 94550

Tel: 925-422-6669
FAX: 925-736-6889
Email: kinney3@llnl.gov

Keywords: trabecular bone, human vertebra, orientation, microtomography, osteoporosis.

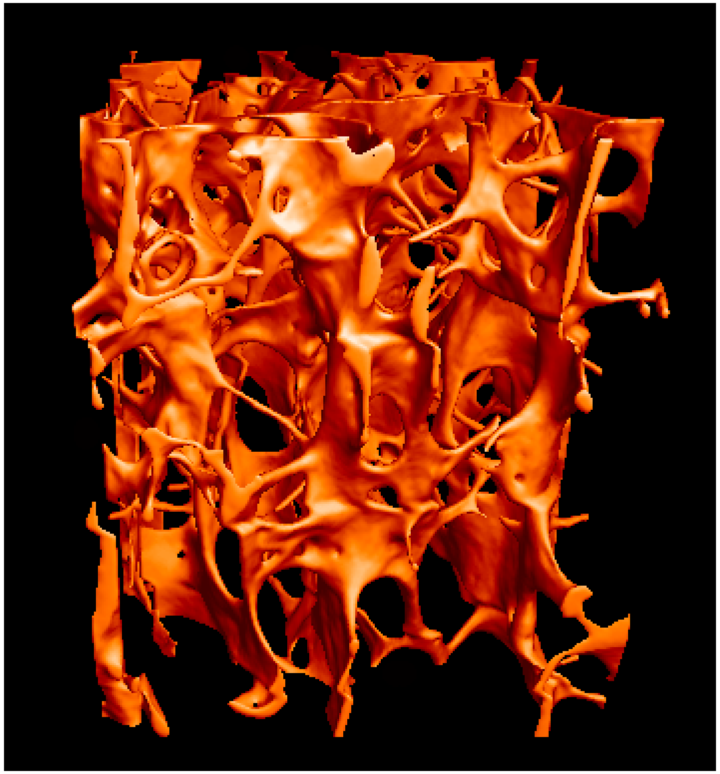

J.H. Kinney et al., Orientation Distribution Function

Figure 1

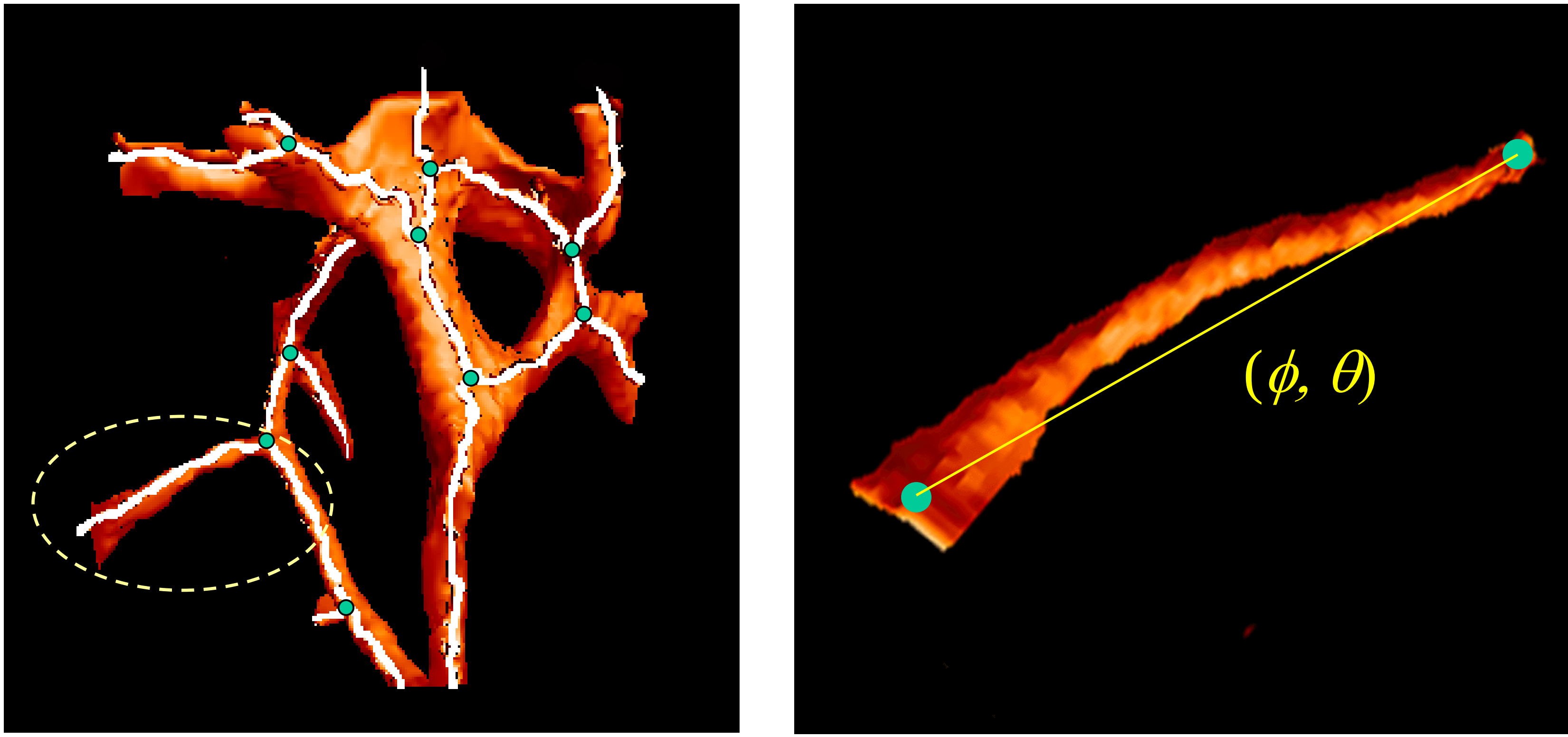

J.H. Kinney et al., Orientation Distribution Function

Figure 2a,b

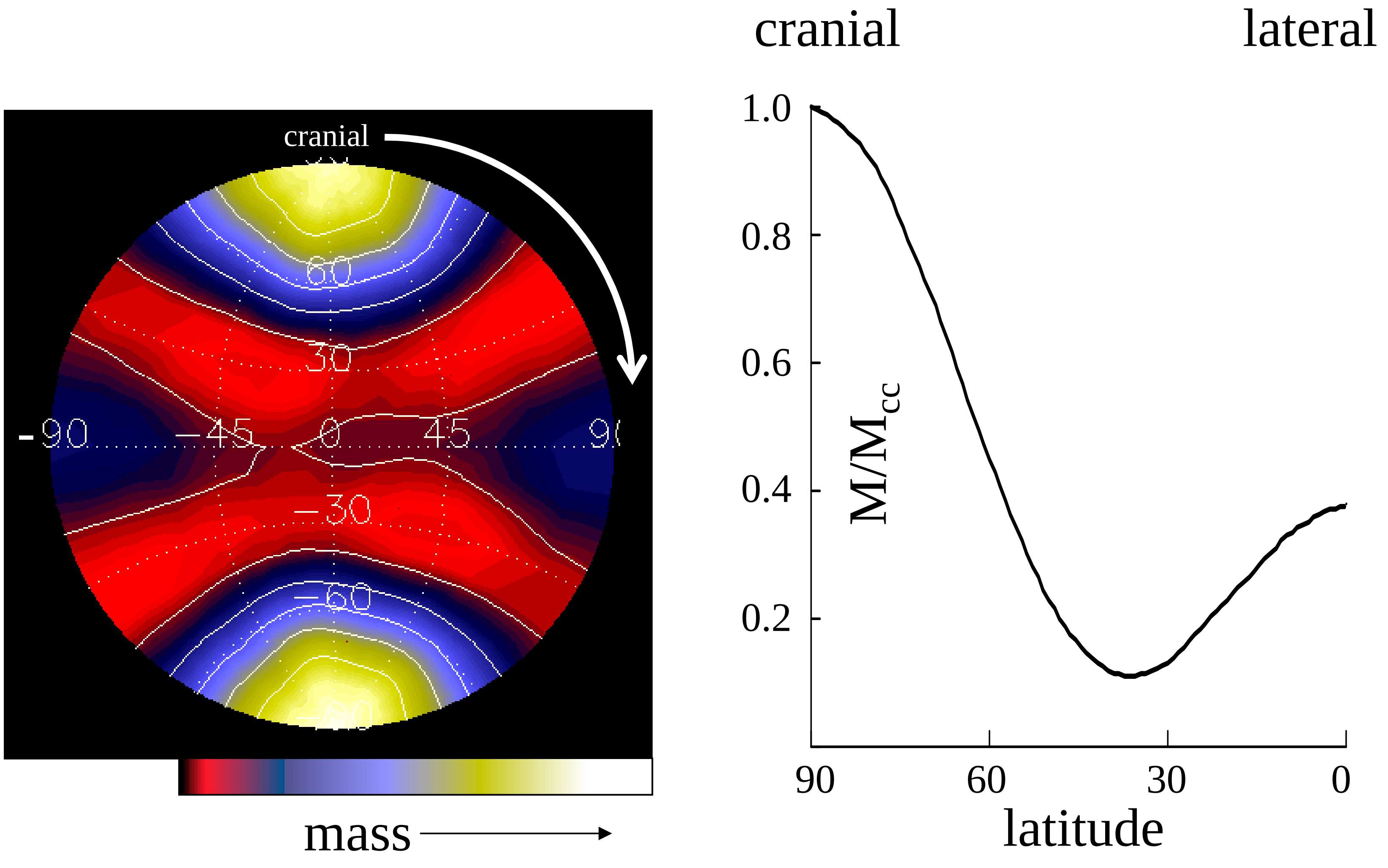

J.H. Kinney et al., Orientation Distribution Function

Figure 3a,b

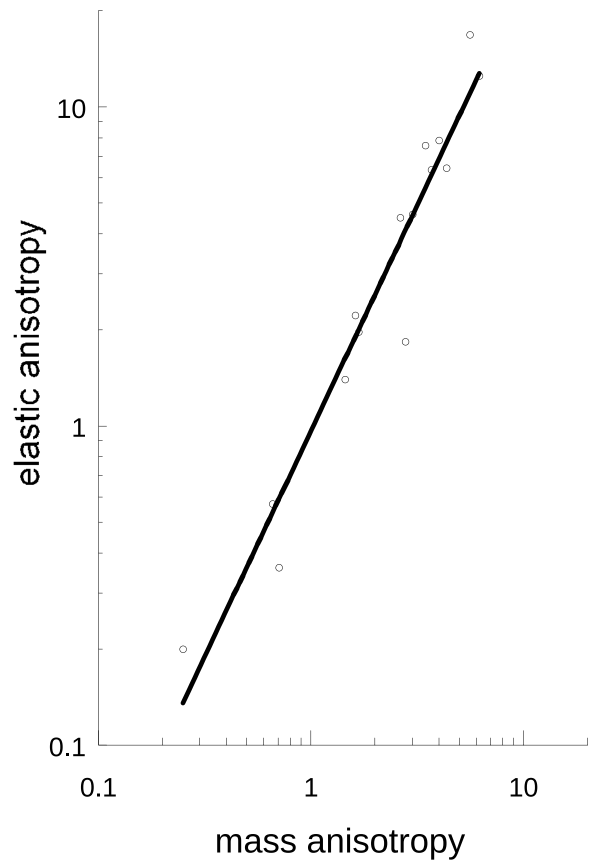

J.H. Kinney et al., Orientation Distribution Function

Figure 4

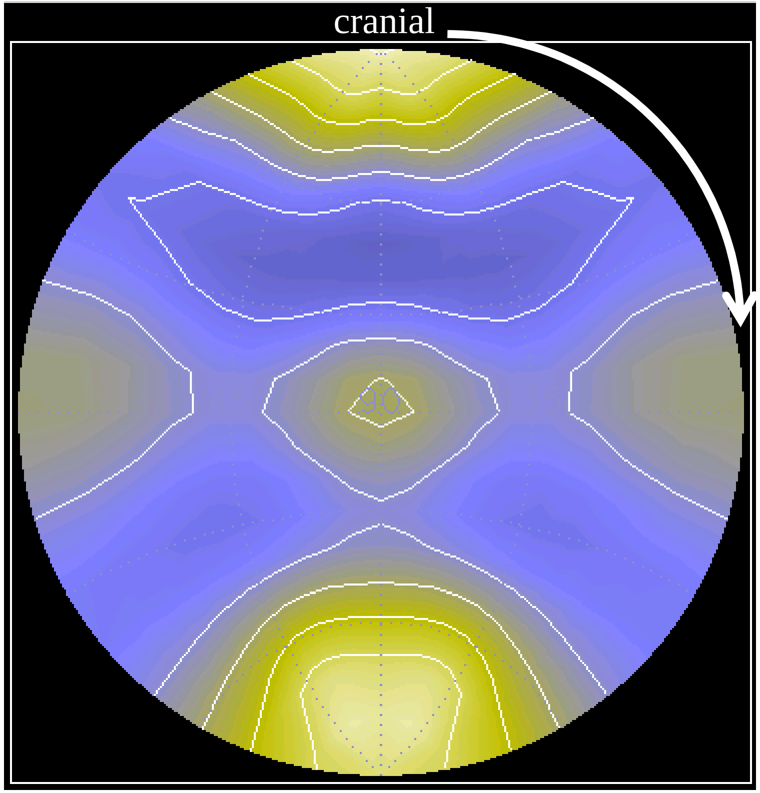

cranial
90

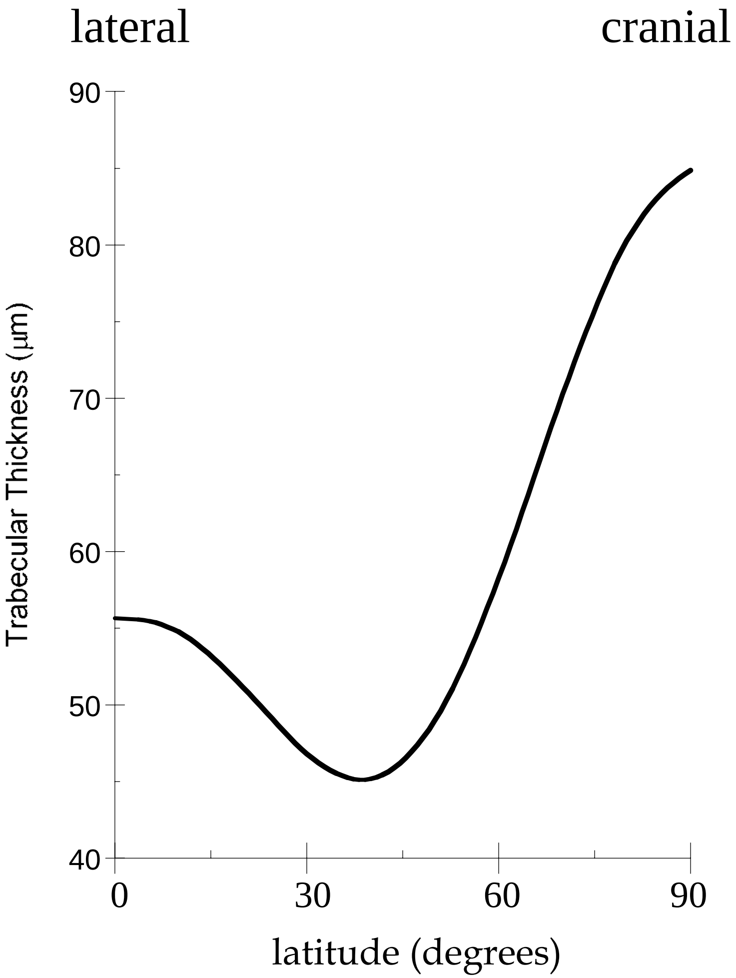

lateral
cranial
Trabecular Thickness (µm)
90
80
70
60
50
40
0
30
60
90
latitude (degrees)

Figure 5a.b

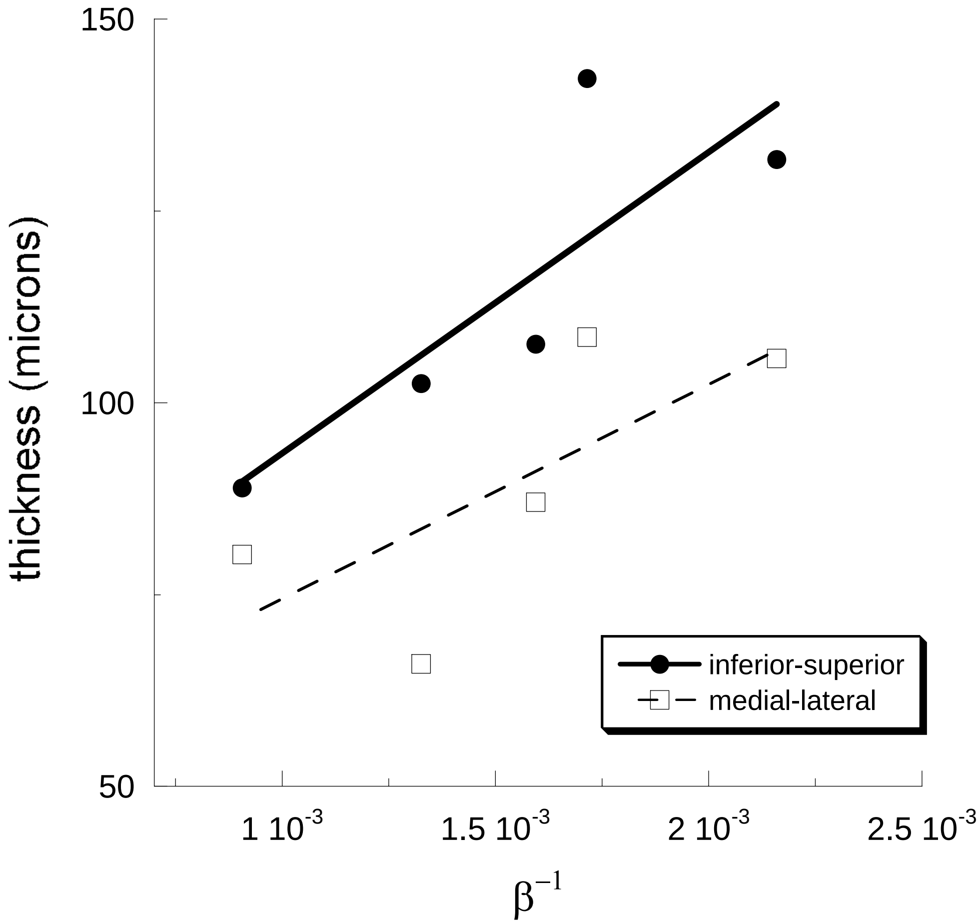

J.H. Kinney et al., Orientation Distribution Function

Figure 6

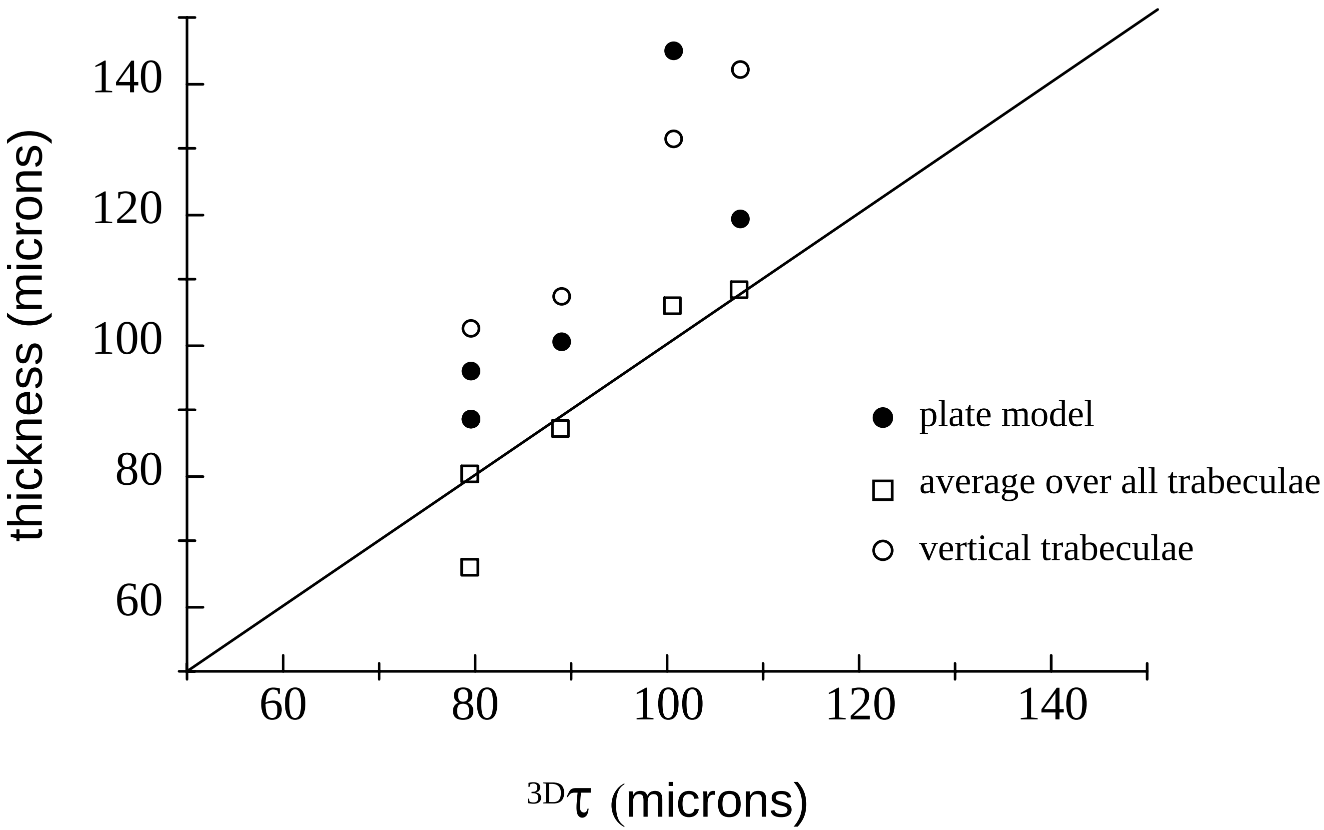

thickness (microns)
140
120
100
80
60
60
80
100
120
140
$^{3D}\tau$ (microns)
plate model
average over all trabeculae
vertical trabeculae

Figure 7

a

b

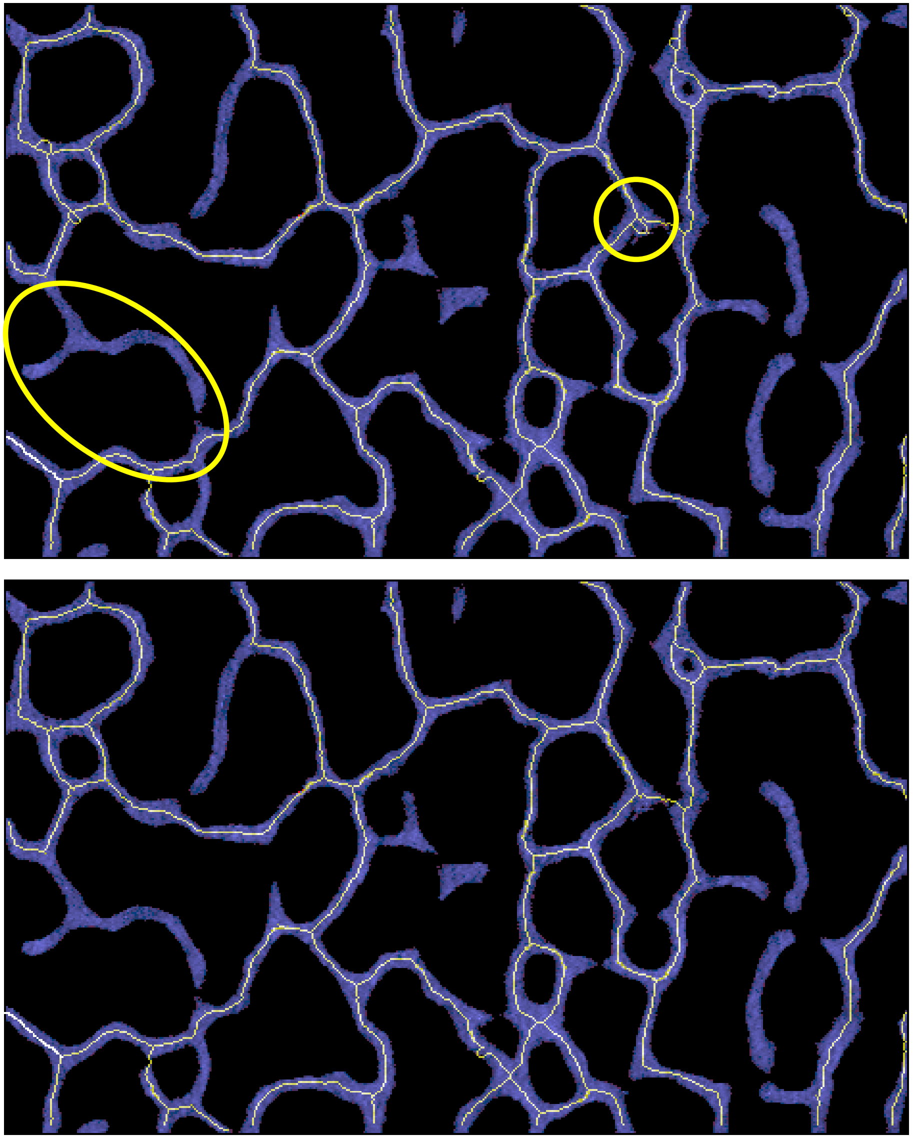

Figure 8

c

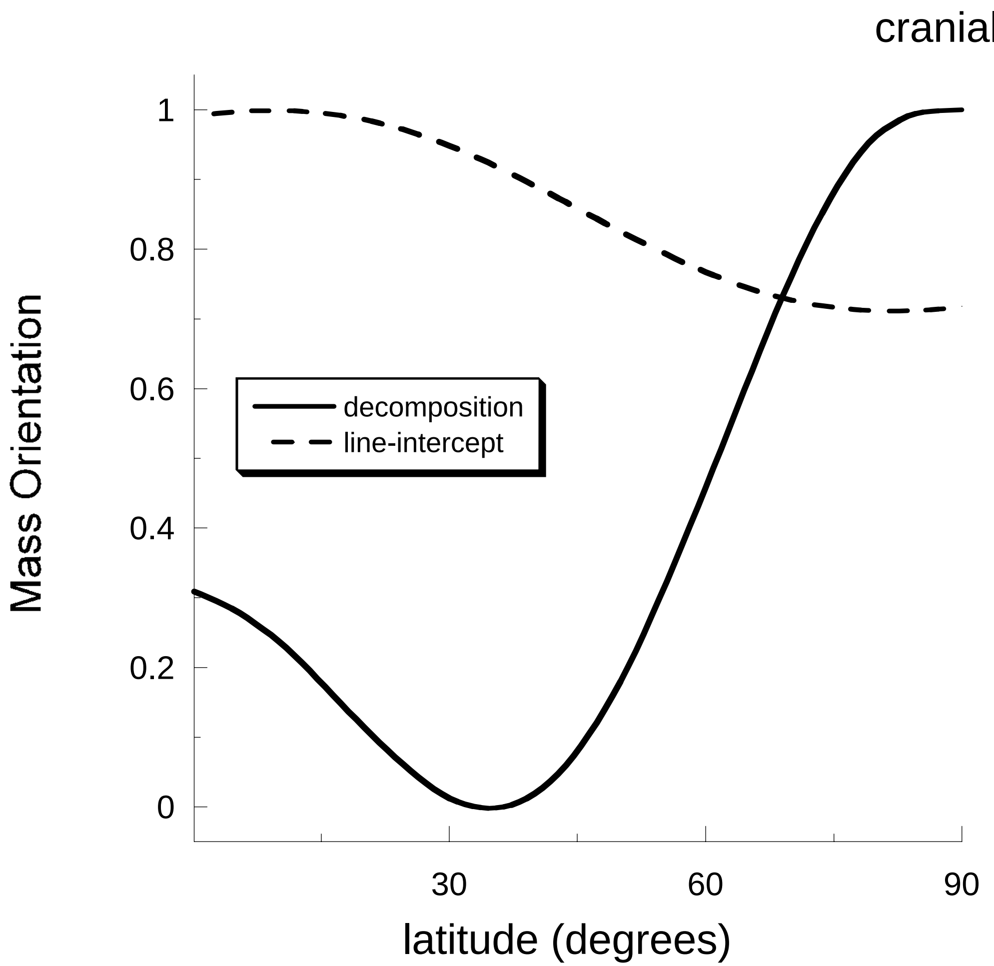
cranial
Mass Orientation
1
0.8
0.6
0.4
0.2
0
30
60
90
latitude (degrees)
decomposition
line-intercept

Abstract

We describe a new method for quantifying the orientation of trabecular bone from three–dimensional images. Trabecular lattices from five human vertebrae were decomposed into individual trabecular elements, and the orientation, mass, and thickness of each element were recorded. Continuous functions that described the total mass ($\boldsymbol{M}(\varphi,\theta)$) and mean thickness ($\tau(\varphi,\theta)$) of all trabeculae as a function of orientation were derived. The results were compared with experimental measurements of the elastic modulus in the three principal anatomic directions. A power law scaling relationship between the anisotropies in mass and elastic modulus was observed; the scaling exponent was 1.41 (R^2 = 0.88). As expected, the preponderance of trabecular mass was oriented along the cranial–caudal direction; on average, there was 3.4 times more mass oriented vertically than horizontally. Moreover, the vertical trabeculae were 30% thicker, on average, than the horizontal trabeculae. The vertical trabecular thickness was inversely related to the connectivity (R^2 = 0.70; p = 0.07), suggesting a possible organization into either few, thick trabeculae or many thin trabeculae. The method, whichaccounts for the mechanical connectedness of the lattice, provides a rapid way to both visualize and quantify the three-dimensional organization of trabecular bone.

Running Title: ODF for Trabecular Bone

Introduction

The increased risk of fracture following estrogen reduction at menopause is linked with loss of bone mass (33). However, bone mass is not perfectly correlated with fracture; there is significant overlap of normal and osteoporotic populations when fracture frequency is compared (14, 34). To explain this overlap, investigators have proposed risk factors in addition to bone mass, such as deterioration of trabecular architecture (22).

Relating trabecular architecture to fracture risk is difficult. Trabecular bone is a dynamic system; its architecture can adaptively compensate for local deficiencies in strength through remodeling or micro–modeling (5). These dynamic adaptations confound attempts to correlate architecture with mechanical behavior. In addition, trabecular bone’s anisotropy plays a critical role in its biomechanical behavior (11). When the preferred orientation of trabecular bone is accounted for in a fabric tensor, there is a marked improvement in predicting stiffness and strength (3). Therefore, in studies of trabecular bone loss with aging and menopause, it becomes important to measure not only trabecular bone mass, but to record where and along what orientation the bone is lost or gained in response to altered mechanical set points. Such studies are now feasible due to the development of instrumentation for three–dimensional imaging of trabecular bone (6, 20, 27), and of techniques for finite-element modeling from these images (23, 28, 38, 39).

We present a method for describing the orientation of trabecular bone that is based on its decomposition into individual structural elements. The method, which takes as its starting point the skeletal decomposition method described by Pothuaud et al. (31, 32), allows characterization of the microstructure of individual trabeculae. We used this method to examine the orientation dependence of trabecular architecture in specimens of human vertebrae. We compared the mass anisotropy with the orientation dependence of the elastic modulus. In addition, the thickness of trabeculae lying along different orientations was measured. These measurements of individual trabecular elements were compared with conventional measures of trabecular thickness.

Materials and Methods

Specimen preparation and imaging

Five cubic specimens of trabecular bone, which had been used in earlier studies (19), were prepared from human L1 vertebrae. Human subjects exemption had been granted by the Lawrence Livermore National Laboratory's Institutional Review Board. The specimens were cut under irrigation with a slow speed diamond saw from the superior–anterior region to a dimension of 8 mm. The orientations of the cubes with respect to the principal anatomic axes were noted. The vertebrae were from males aged 63–80 years.

After preparation, the specimens were imaged with synchrotron radiation. The specimens were oriented with the cranial surface on top, and with the detector facing the posterior surface at zero degrees of axis rotation. The radiation was monochromatic at 25 keV. Tomography was performed according to a protocol described in detail elsewhere (17, 18, 21). Two–dimensional radiographs of the specimens were obtained at half–degree rotational increments, and the data were reconstructed into three–dimensional images by Fourier–filtered back–projection. For this study, the data were reconstructed into cubic volume elements (voxels) 11.7 μm on edge. A 4 mm subset of a typical CT image is shown in Figure 1.

Image processing and analysis

To decompose the lattice of trabecular bone into its individual structural elements, it was first necessary to remove the marrow from the images. Setting all image voxels below a marrow threshold to zero accomplished this task. Monochromatic radiation provided high contrast between the marrow and bone tissue; therefore, a single threshold could be used for segmentation (18).

After segmentation, the images were skeletonized with a requirement that connectivity be preserved. All surface voxels were identified, and then removed. If the removal of a voxel would have altered the connectivity, then it was forced to remain. This peeling operation was repeated until elements could no longer be removed. A magnified region of trabecular bone, with its skeleton superposed, is shown in Figure 2a.

The medial line segments that composed the skeleton did not always converge to a common vertex. This created many closely spaced nodes and short line segments that, upon closer inspection, were artifacts of the skeletonization (e.g., see Figure 8). Therefore, nodes that were within a mean trabecular thickness of one another were merged.

After skeletonizing, every trabecular element was removed from the lattice at its nodal points (Figure 2b); the mass (assuming a uniform density for each voxel), length, and thickness at midpoint of each of these trabecular elements were recorded. Two measures of trabecular length were recorded: Euclidian length (EL), defined as the straight-line distance between nodal points, and the length of the skeletal line segment (CL). By comparing the ratios of these two measures, an estimate of trabecular curvature could be obtained. Thickness at midpoint was defined as the smallest diameter sphere that could fit within the trabecular element at a position midway between the nodes.

The orientation of each trabecular element was defined by its angular tilt, θ, and azimuthal angle, ϕ, with respect to the posterior surface. The coordinates were defined with the cranial direction at 90 degrees tilt (North Pole), and the posterior direction at zero degrees azimuth (longitude) and zero degrees tilt (latitude). The lateral and anterior/posterior directions lay on the equatorial plane.

The mass of each trabecular element was recorded on the surface of a sphere, with its latitude (θ) and longitude (ϕ) defining its position in the upper hemisphere. The mass was also recorded at its mirror position in the lower hemisphere to preserve spherical symmetry. A continuous function, the mass orientation distribution function, $M(\phi,\theta)$, was fit to the discrete points (scalar field) distributed on the sphere (see Appendix). The spherical representation of the data made it natural to define $M(\phi,\theta)$ in terms of a series of spherical harmonics (see appendix). A similar function, $\tau(\phi,\theta)$ defined a thickness orientation distribution function. Here, instead of summing all the mass, the mean thickness of all trabecular elements oriented along ϕ,θ was recorded.

As the spherical harmonic representation is an infinite series expansion, in principal the distribution functions could be forced to fit every point of the scalar field. However, because trabecular bone appears to be orthotropic we chose to limit the terms of the expansion to 6th order. This was sufficient to fit the three principal directions as well as distinguish deviations from orthotropic symmetry. However, the fit overestimated the contributions from the 20% or so of the mass that was oriented aw from an axis of symmetry. The fits in these regions were improved by adding additional terms to the expansion, but as this did not improve the correlations with the elastic properties, we decided to limit the expansion to 6^{th} order.

Histomorphometric analyses

For comparison, a spatially averaged trabecular thickness was estimated in two ways. First, a biased mean trabecular width (Tb.Th) was estimated with the plate model from a single coronal cross section through the middle of each specimen. Second, an unbiased mean trabecular thickness $^{3D}\langle\tau\rangle$ was obtained from the relationship between surface area, *S*, and volume, *V*, in three–dimensions (40):

$$^{3D}\langle\tau\rangle = \frac{2V}{S} \qquad (1)$$

Here, the surface area was determined by integrating a polygonal surface mesh, and trabecular volume was determined by voxel counting.

Three–dimensional connectivity, $^{3D}\beta_1$, was determined with Feldkamp's algorithm (6) after image purification. Image purification (29) removed the isolated packets of bone and marrow (salt and pepper noise at the trabecular surfaces) that were an unavoidable consequence of image segmentation. Though the total volume of these packets was inconsequential ($< 10^{-5}$ of the total bone volume), their number was high enough to measurably affect the connectivity density (29).

Finite-element simulations

The image voxels were converted into finite elements, and the Young's modulus was determined for each of the three orthogonal orientations. The elements preserved the same dimensionality as the image voxels, 11.7 μm on edge. The element-by-element algorithm, originally formulated by Hughes et al. (13), was adapted for the analysis. The element type was the lattice-spring element described elsewhere (24, 25). An isotropic, linear elastic constitutive model with the tissue modulus normalized to 1 GPa and a Poisson's ratio of 0.3 was used for the computations. For computational efficiency, the solutions were confined to the original lattice configuration; the linear kinematic approximation is believed to be valid for small strain determinations of the elastic response of trabecular bone (36).

Results

The mass anisotropy of each specimen is given in Table 1. A representative mass orientation distribution function, $M(\phi,\theta)$, is shown in Figure 3a. A color table represents the magnitude of M, with black to red being the lowest values and yellow–white being the highest. Orthotropic (three perpendicular mirror planes) symmetry was apparent in the mass orientation distribution functions. The mass distribution is graphed along a line of constant longitude ($\theta = +90^{o}$) between the cranial and lateral directions in Figure 3b. On average, there was 3.4 (s.d. = 0.49) times more mass oriented vertically (in the cranial/caudal direction) than horizontally (in the medial/lateral direction). This anisotropy in mass orientation was independent of the total amount of cancellous bone.

The ratios of mass in the three orthogonal directions (mass anisotropy A_M) are graphed against the measured ratios of the elastic modulus (elastic anisotropy A_E) in Figure 4. The data followed a power law relationship with a scaling exponent $\gamma = 1.41$ ($R^2 = .88$):

$$A_E \propto \left(A_M\right)^{\gamma} \qquad (2)$$

The thickness distribution function $\tau(\phi,\theta)$ of a different specimen is shown in Figure 5a. The thickness distribution for a constant longitude ($\theta = +90^{o}$) is graphed between the cranial and lateral orientations in Figure 5b. The thickest trabeculae were oriented along the load-bearing axis. Trabecular thickness and the reciprocal of the connectivity were correlated, as shown in Figure 6. The correlation was strongest along the vertical orientation ($R^2 = 0.70$; $p = 0.07$), and weaker for the horizontal trabeculae ($R^2 = 0.53$; $p = 0.16$). This correlation between connectivity and thickness was observed in the absence of any correlation between trabecular bone volume and connectivity.

The trabecular thickness determined with the plate model, Tb.Th, was compared with the unbiased three–dimensional measure of thickness. As shown in Figure 7, the thickness determined with the plate model always overestimated the three–dimensional value. The plate model thickness more closely paralleled the thickness of the vertical plates.

Discussion

We have developed an orientation distribution function for trabecular bone that is based on its decomposition into individual structural elements. We have applied this function to the analysis of three–dimensional synchrotron radiation microtomography images of trabecular bone from human vertebrae. In spite of the small number of specimens, several observations merit discussion.

As expected, the preponderance of trabecular mass was oriented vertically, and its distribution was generally orthotropic. More important, the anisotropy in mass did not depend on trabecular bone volume. All of the orientation distribution functions were similar in appearance, suggesting that the anisotropy of cancellous bone in the vertebra might be invariant with respect to bone density. Thus, we have provided additional supporting evidence of an earlier observation by Fyhrie et al. that cancellous bone tends to maintain constant ratio of trabecular number along principal axes (8), and more recent observations by Yang, et al. (43) that the eigenvectors (i.e., the principal axes in a tensoral analysis of linear elasticity) are independent of bone volume. It remains to be seen whether osteoporotic bone retains this symmetry, or whether the symmetry might be altered by pathologies affecting bone turnover.

The measured anisotropy in Young's modulus, A_E, was related by a power law to the anisotropy in mass, A_M, when the same orientations were compared. This was not entirely unexpected; fabric tensor analysis based on the orientation dependence of mean intercept lengths is an effective predictor of elastic anisotropy (3). In addition, there is a theoretical basis for a power law relationship between elastic modulus and apparent density, ρ_a, based on the likely deformation mechanisms in low–density foams (9, 10). For low–density foams, it is established that the Young's modulus, E, scales as

$$E \propto (\rho_a)^\gamma \qquad (3)$$

where $\rho_a = \rho/\rho_s$, and ρ_s is the density of the solid. Theoretical arguments justify limiting values of $\gamma = 1$ for a perfect closed–cell foam, and $\gamma = 2$ for a perfect open–cell foam (2). Keaveny and Hayes (16) have reported a value of $\gamma = 1.44$ for trabecular bone.

However, a scaling law that relates the average apparent density with a spatially averaged material property does not imply that A_E and A_M should scale with the same exponent, particularly in a heterogeneous material. That it appears to do so is an indication that, for small strain elastic deformations, there is little or no coupling between the principal anatomic orientations. Coupling will no doubt arise at greater strains, although this can only be tested with geometrically nonlinear finite element simulations (36).

As shown in Figure 6, trabecular thickness appeared to be correlated with the reciprocal of the connectivity. In other words, trabecular bone seems to be organized into either a few thick trabeculae or many thin trabeculae. This correlation appeared strongest for trabeculae oriented vertically. We can think of three reasons for this relationship. First, a uniform thinning of trabecular plates would initially increase the number of plate fenestrations and give the appearance of an increase in connectivity (18). This would also be consistent with correlation being strongest in the vertical (more plate–like) orientation. Second, the preferential removal of the thinnest trabecular elements would also give the appearance that the mean trabecular thickness increases as connectivity (or trabecular number) decreases (7). Third, micromodeling, whereby the vertical trabeculae thicken to compensate for their fewer numbers, would also be consistent with our observations (5), although the evidence supporting this effect has largely been anecdotal (15, 42).

In this study, the two-dimensional plate model measure of trabecular thickness, Tb.Th, always overestimated the thickness determined by the 3D method. This was in contrast to an earlier study by Day et al. (4), who observed the opposite behavior. The difference between our work and theirs was that we measured the 2D Tb.Th. from a single coronal section, which was biased in favor of the thicker vertical trabeculae. A better procedure for estimating 2D Tb.Th would have been to take random, unbiased sections from different orientations (4). Unfortunately, this is rarely done in practice, especially in small animal studies where there is little available bone to utilize. With three–dimensional imaging methods, this bias was removed.

Three–dimensional imaging of trabecular bone is more common now that high-resolution scanners have become available (1, 20, 21, 27, 29, 35). However, with few exceptions the methods of structure analysis have not taken full advantage of three–dimensionality. The exceptions are important: three–dimensional measures of connectivity (a measure of topology) (6), the structure model index (a measure of shape) (12), and fractal dimension (a measure of complexity) (37) have improved our understanding of trabecular bone architecture. With respect to trabecular orientation, however, present methods of analysis have relied on extensions of the line intercept method or its equivalent in the Fourier transform domain (29, 30, 41). The intercept method, which assumes mechanical coupling of the lattice, is a statistical measure of orientation. It provides a spatially averaged estimate of trabecular thickness that does not discriminate between horizontal and vertical orientations. We believe that the skeleton–based, structural decomposition method proposed here, which provides a catalogue of all trabecular elements in the specimen, offers a significant improvement over line intercept methods for only a fractional increase in computational effort.

The line intercept method provides a statistical sampling o the trabecular mass, and provides a measure of how this mass is oriented in the bone. However, line intercepts cannot discriminate between connected or disconnected trabecular segments, thereby being insensitive to changes in connectivity that might affect the mechanical response. This problem is illustrated in Figure 8, where fenestrated trabeculae that are uncoupled mechanically are removed from the skeletal representation but would still be included in a line-intercept sampling. Thus, the orientation distribution function proposed here provides a measure of the "structural" symmetry as opposed to simply the average orientation of the mass.

Another advantage of the proposed orientation distribution function, which arises from the skeletal decomposition, is the ability to quantify the thickness of trabecular members oriented in a given direction. Thus, preferential thinning of horizontal trabeculae, out of proportion to the members oriented vertically, could be detected with the proposed method. As the line intercept method can only provide a mean thickness averaged over all of the trabecular elements, it cannot be used to reliably determine anisotropy in thickness. Thus, we believe that our proposed distribution function will be ore sensitive to architectural changes that might affect strength than more traditional methods based on the line intercept technique.

A shortcoming with our study was the small number of specimens that were imaged. These specimens were chosen because we had mechanical data for them (23). Further studies on more specimens from different genders and a greater range in age will be required before we can discuss the present results within the broader context of aging and osteoporosis.

In summary, we have introduced a three–dimensional method for describing the orientation of trabecular structure. The method attempts to reintroduce an architectural framework into voxel–based image representations of cancellous bone. There are still improvements that could be made to the method. Particularly, the decomposition of plate–like structures into beam elements is somewhat arbitrary, and may lead to dispersion in the orientation distribution function. Nevertheless, we believe that the decomposition of cancellous architecture into its individual trabecular elements, and a spherical harmonic representation of this data, will provide a tool to help answer long standing questions about how deterioration of trabecular bone architecture contributes to the increased risk of fracture associated with osteoporosis.

Acknowledgments

The experimental work was performed at Stanford Synchrotron Radiation Laboratory, Stanford, CA, and on the tomography beamline 8.3.2 at the Advanced Light Source, Berkeley, CA. Both facilities are supported by the U.S. Department of Energy. The ALS is supported under contract DE-AC03-76SF00098; SSRL is supported under contract DE-AC03-76SF00515. Work at Livermore was supported by the Laboratory Science and Technology Office, LDRD-04-LW-005. Additional support provided by NIH/NIAMS 2RO1-AR043052-07 (NEL). The work was performed under the auspices of the U.S. Department of Energy by the University of California, Lawrence Livermore National Laboratory under Contract No. W-7405-ENG-48.

References

1. Bonse, U., and Busch, F. X-ray computed microtomography (microCT) using synchrotron radiation (SR). Progress in Biophysics and Molecular Biology 65*:*133-169; 1996.
2. Christensen, R. M. The hierarchy of microstructures for low density materials. Zeitschrift fur Angewandte Mathematik und Physik 46*:*S506-S521; 1995.
3. Cowin, S. C. The relationship between the elasticity tensor and the fabric tensor. Mechanics of Materials 4*:*137-147; 1985.
4. Day, J. S., Ding, M., Odgaard, A., Sumner, D. R., Hvid, I., and Weinans, H. parallel plate model for trabecular bone exhibits volume fraction-dependent bias. Bone 27*:*715-720; 2000.
5. Erben, R. G. Trabecular and endocortical bone surfaces in the rat: Modeling or remodeling? Anatomical Record 246*:*39-46; 1996.
6. Feldkamp, L. A., Goldstein, S. A., Parfitt, A. M., Jesion, G., and Kleerekoper, M. The direct examination of three-dimensional bone architecture in vitro by computed tomography. Journal of Bone and Mineral Research 4*:*3-11; 1989.
7. Frost, H. M. Perspectives on the trabecular "thickness"-number problem. Journal of Bone and Mineral Research 14*:*1816-1821; 1999.
8. Fyhrie, D. P., Lang, S. M., Hoshaw, S. J., Schaffler, M. B., and Kuo, R. F. Human vertebral cancellous bone surface distribution. Bone 17*:*287-91; 1995.
9. Gibson, L. J., and Ashby, M. F. Cellular Solids: Structure and Properties. Oxford: Pergamon; 1988.
10. Gibson, L. J., and Ashby, M. F. The mechanics of three-dimensional cellular materials. Proceedings of the Royal Society London A382*:*43-59; 1982.
11. Harrigan, R. P., and Mann, R. W. Characterization of microstructural anisotropy in orthotropic materials using a second rank tensor. Journal of Materials Science 19*:*761-767; 1984.
12. Hildebrand, T., and Ruegsegger, P. Quantification of bone microarchitecture with the structure model index. Computer Methods in Biology and Bioengineering 1*:*15-23; 1997.
13. Hughes, T., Levit, I., and Winget, J. An element by element solution algorithm for problems of structural and solid mechanics. Mechanics and Engineering 36*:*241-254; 1983.
14. Hui, S. L., Slemenda, C. W., and Johnston, C. C. Age and bone mass as predictors of fracture in a prospective study. Journal of Clinical Investigations 81*:*1804-1809; 1988.
15. Jayasinghe, J. A. P., Jones, S. J., and Boyde, A. Three-dimensional photographic study of cancellous bone in human fourth lumbar vertebral bodies. Anatomy and Embryology 189*:*259-274; 1994.
16. Keaveny, T. M., and Hayes, W. C. A 20-year perspective on the mechanical properties of trabecular bone. J Biomech Eng 115*:*534-42; 1993.
17. King, W. E., Campbell, G. H., Haupt, D. L., Kinney, J. H., Riddle, R. A., and Wien, W. L. X-Ray Tomographic Microscopy Investigation of the Ductile Rupture of an Aluminum Foil Bonded between Sapphire Blocks. Scripta Metallurgica Et Materialia 33*:*1941-1946; 1995.

18. Kinney, J. H., Haupt, D. L., Balooch, M., Ladd, A. J. C., Ryaby, J. T., and Lane, N. E. Three-dimensional morphometry of the L6 vertebra in the ovariectomized rat model of osteoporosis: Biomechanical implications. Journal of Bone and Mineral Research 15*:*1981-1991; 2000.
19. Kinney, J. H., and Ladd, A. J. C. The relationship between three-dimensional connectivity and the elastic properties of trabecular bone. Journal of Bone and Mineral Research 13*:*839-845; 1998.
20. Kinney, J. H., Lane, N. E., and Haupt, D. L. In vivo, three-dimensional microscopy of trabecular bone. J Bone Miner Res 10*:*264-70; 1995.
21. Kinney, J. H., and Nichols, M. C. X-Ray Tomographic Microscopy (XTM) Using Synchrotron Radiation. Annual Review of Materials Science 22*:*121-152; 1992.
22. Kleerekoper, M., Villanueva, A. R., Stanciu, J., Rao, S., and Parfitt, A. M. The role of three-dimensional trabecular microstructure in the pathogenesis of vertebral compression fractures. Calcified Tissue Research 37*:*594-597; 1985.
23. Ladd, A. J., Kinney, J. H., Haupt, D. L., and Goldstein, S. A. Finite-element modeling of trabecular bone: comparison with mechanical testing and determination of tissue modulus. J Orthop Res 16*:*622-8; 1998.
24. Ladd, A. J. C., and Kinney, J. H. Elastic constants of cellular structures. Physica A 240*:*349-360; 1997.
25. Ladd, A. J. C., Kinney, J. H., and Breunig, T. M. Deformation and failure in cellular materials. Physical Review E 55*:*3271-3275; 1997.
26. Morse, P. M., and Feshbach, H. Methods of Theoretical Physics. New York: McGraw-Hill; 1953.
27. Muller, R., Hildebrand, T., and Ruegsegger, P. Non-invasive bone biopsy: a new method to analyze and display three-dimensional structure of trabecular bone. Physics in Medicine and Biology 39*:*145-164; 1994.
28. Niebur, G. L., Yuen, J. C., Hsia, A. C., and Keaveny, T. M. Convergence behavior of high-resolution finite element models of trabecular bone. J Biomech Eng 121*:*629-35; 1999.
29. Odgaard, A. Three-dimensional methods for quantification of cancellous bone architecture. Bone 20*:*315-328; 1997.
30. Odgaard, A., Jensen, E. B., and Gundersen, H. J. Estimation of structural anisotropy based on volume orientation. A new concept. Journal of Microscopy-Oxford 157*:*149-162; 1990.
31. Pothuaud, L., Laib, A., Levitz, P., Benhamou, C. L., and Majumdar, S. Three-dimensional-line skeleton graph analysis of high-resolution magnetic resonance images: a validation study from 34-microm-resolution microcomputed tomography. J Bone Miner Res 17*:*1883-95; 2002.
32. Pothuaud, L., Porion, P., Lespessailles, E., Benhamou, C. L., and Levitz, P. A new method for three-dimensional skeleton graph analysis of porous media: application to trabecular bone microarchitecture. J Microsc 199 (Pt 2)*:*149-61; 2000.
33. Riggs, B. L., and Melton, L. J. Evidence for two distinct syndromes in involutional osteoporosis. American Journal of Medicine 75*:*899-901; 1983.

34. Ross, P. D., Kress, B. C., Parson, R. E., Wasnich, R. D., K.A., A., and Mizrahi, I. A. Serum bone alkaline phosphatase and calcaneus bone density predict fractures: a prospective study. Osteoporos Int 11:76-82; 2000.
35. Ruegsegger, P., Koller, B., and Muller, R. A microtomographic system for the nondestructive evauation of bone architecture. Calcified Tissue International 58:24-29; 1996.
36. Stolken, J. S., and Kinney, J. H. On the importance of geometric nonlinearity in finite-element simulations of trabecular bone failure. Bone 33:494-504; 2003.
37. Uchiyama, T., Tanizawa, T., Muramatsu, H., Endo, N., Takahashi, H. E., and Hara, T. Three-dimensional microstructural analysis of human trabecular bone in relation to its mechanical properties. Bone 25:487-491; 1999.
38. Ulrich, D., van Rietbergen, B., Weinans, H., and Ruegsegger, P. Finite element analysis of trabecular bone structure: a comparison of image-based meshing techniques. J Biomech 31:1187-92; 1998.
39. van Rietbergen, B. Micro-FE analyses of bone: state of the art. Adv Exp Med Biol 496:21-30; 2001.
40. Weibel, E. R. Stereological Methods. San Diego: Academic Press; 1989.
41. Whitehouse, W. J. The quantitative morphology of anisotropic trabecular bone. Journal of Microscopy-Oxford 101:153-168; 1974.
42. Wu, D. D., Burr, D. B., Boyd, R. D., and Radin, E. L. Bone and cartilage changes following experimental varus or valgus tibial angulation. Journal of Orthopaedic Research 8:572-585; 1990.
43. Yang, G., Kabel, J., van Rietbergen, B., Odgaard, A., Huiskes, R., and Cowin, S. C. The anisotropic Hooke's law for cancellous bone and wood. J Elast 53:125-46; 1998.

Table 1: The mass anisotropy for three orthogonal orientations, of which, only two are independent. M_{cc}/M_{ap} is the ratio of the total mass oriented in the cranial–caudal direction (cc) to the total mass oriented in the anterior–posterior direction (ap). M_{ml} is the mass oriented in the lateral direction.

	Orientation		
Specimen	$\mathbf{M_{cc}/M_{ap}}$	$\mathbf{M_{cc}/M_{ml}}$	$\mathbf{M_{ml}/M_{ap}}$
532	3.5	5.6	0.6
533	3.0	4.4	0.7
534	3.7	6.2	0.6
535	2.8	0.7	0.3
536	4.0	2.6	1.5

List of Figure Captions

1. A representative synchrotron microtomography image of a cube of trabecular bone reconstructed into 11.7 μm voxels. For improved clarity, only the interior 4–mm of the cube has been displayed in this image. The trabecular lattice is a complex arrangement of plates and beams.

2. A) small section of trabecular bone from the cube displayed in Figure 1 with skeleton superposed. The skeleton has been thickened by one to two voxels to improve visibility. The nodes (green circles) appear at the intersection of two or more line segments. B) the trabecular element circled in 2A in greater detail after its removal from the lattice. The angles (ϕ,θ) of the straight–line segment connecting the nodes define the orientation of the trabecular element with respect to the anatomic axis.
3. A mass orientation distribution function, $\boldsymbol{M}$, of a representative specimen is shown in the image on the left (3a). The yellow–white color spectrum represents a greater amount of mass than the red–blue colors. The viewpoint is from the posterior direction. The mass distribution is graphed along a line of constant longitude (+90^{o}) between the cranial and lateral directions in 3b. The graph shows the ratio of the mass at the given latitude to the mass oriented along the cranial–caudal axis, $\boldsymbol{M_{cc}}$.
4. A double-log graph of the ratios of mass in each of the three orthogonal directions (mass anisotropy, $\boldsymbol{A_M}$ in Equation 2) with the corresponding ratios of the elastic modulus (elastic anisotropy, $\boldsymbol{A_E}$). The data can be described by the power law relationship in Equation 2, with the scaling exponent $\gamma = 1.41$ ($R^2 = 0.88$).

5. The orientation distribution function of trabecular thickness (left) viewed from the posterior direction with cranial direction at the top. On the right is graphed the thickness along a path (shown by the arrow) from the cranial (vertical) orientation to the lateral (horizontal) orientation. The vertical trabeculae were much thicker than the horizontal trabeculae. Also, there was a pronounced orthotropic symmetry in the thickness distribution.
6. The mean thickness of the vertical (solid circles) and horizontal (open squares) trabeculae in each specimen graphed as a function of the reciprocal of the connectivity. The higher the connectivity the thinner the trabeculae, implying an organization into either a few thick trabeculae or many thin trabeculae. The correlation was best among the vertical trabeculae ($R^2 = 0.70$).
7. Mean magnitudes of trabecular thickness by various measurement approaches compared with the unbiased three-dimensional average (${}^{3D}\tau$). Open squares are the mean thickness from averaging each individual trabecular element after decomposition. Solid circles are calculated from a single section with the plate model. Open circles are the average thickness of vertical plates alone. For these specimens, the plate model overestimated the mean thickness in all cases.
8. a) merging nodes spaced less than on trabecular thickness (materials and methods) removes artifacts caused in skeletonizing the trabecular lattices. One of many "loops" is highlighted with the small circle. These loops are removed by the merging (8b). The large ellipse highlights one of several tracts of trabeculae that are not mechanically connected in the plane of the image. The trabecular mass associated with these elements would be sampled in the line intercept approach, which does not

account for mechanical connectedness. c) graphical comparison of the line intercept method (dashed line) with the ODF method based on skeletal decomposition (solid line) for the same specimen of trabecular bone. Because the line intercept sampling does not consider the connectedness of the structure, it significantly underestimates the mechanical anisotropy. In addition, the line intercept method misses the almost total absence of trabecular elements oriented at oblique angles to the primary load axis. Note: the line intercept method provides an orthogonal view of the actual mass orientation.

Appendix

Spherical harmonics are a natural choice for describing scalar functions on the surface of a sphere. To derive the continuous orientation functions ***M*** and τ, we used the trigonometric form of the spherical harmonic expansion.(26)

$$M(\varphi,\vartheta)=\sum_{m,n}\left[A_{m,n}Y^{e}_{m,n}(\vartheta,\varphi)+B_{m,n}Y^{o}_{m,n}(\vartheta,\varphi)\right]$$
$$0\le m\le n$$

The spherical harmonics (Y^e and Y^o), which form an orthogonal basis set, are related to the Legendre functions:

$$Y^{e}_{m,n}=\cos(m\varphi)P_n^m(\cos\vartheta)$$
$$Y^{o}_{m,n}=\sin(m\varphi)P_n^m(\cos\vartheta)$$

A generating function was used to derive all of the Legendre functions. For $z=\cos(\theta)$, all of the Legendre functions are given by the following differential expression:

$$P_n^m(z)=\frac{\left(1-z^2\right)^{\frac{m}{2}}}{2^n n!}\frac{d^{m+n}}{dz^{m+n}}\left(z^2-1\right)^n$$

The first three Legendre functions are

$$P_0^0 = 1$$
$$P_1^0 = \cos(\vartheta)$$
$$P_1^1 = \sin(\vartheta)$$

The coefficients $\boldsymbol{A}_{m,n}$ and $\boldsymbol{B}_{m,n}$ were determined by integrating the mass distribution $\boldsymbol{M}$ over the surface of the sphere.

$$A_{m,n} = \frac{(2n+1)\varepsilon_m}{4\pi}\left[\frac{(n-m)!}{(n+m)!}\right]\int_0^{2\pi} d\varphi \int_0^{\pi} MY_{mn}^{e} \sin(\vartheta)\, d\vartheta$$

In the above expression, $\varepsilon_0 = 1$, and $\varepsilon_n = 2$ (n = 1,2,3…). A similar expression determines $\boldsymbol{B}_{m,n}$, but with terms in m = 0 omitted:

$$B_{m,n} = \frac{(2n+1)\varepsilon_m}{4\pi}\left[\frac{(n-m)!}{(n+m)!}\right]\int_0^{2\pi} d\varphi \int_0^{\pi} MY_{mn}^{o} \sin(\vartheta)\, d\vartheta$$